ACS APPLIED MATERIALS & INTERFACES

Research Article

Cite This: ACS Appl. Mater. Interfaces XXXX, XXX, XXX−XXX

www.acsami.org

$LiCrS_2$ and $LiMnS_2$ Cathodes with Extraordinary Mixed Electron−Ion Conductivities and Favorable Interfacial Compatibilities with Sulfide Electrolyte

Zhen-Ming Xu, Shou-Hang Bo, and Hong Zhu*

University of Michigan−Shanghai Jiao Tong University Joint Institute, Shanghai Jiao Tong University, 800, Dongchuan Road, Shanghai 200240, China

Supporting Information

ABSTRACT: Sulfide-type solid-state electrolytes for all-solid-state lithium ion batteries are capturing more and more attention. However, the electronegativity difference between the oxygen and the sulfur element makes sulfide-type solid-state electrolytes chemically incompatible with the conventional $LiCoO_2$ cathode. In this work, we proposed a series of chalcopyrite-structured sulfide-type materials and systematically assessed their performances as the cathode materials in all-solid-state lithium ion batteries by first-principle calculations. All the five metallic $LiMS_2$ (M = Cr, Mn, Fe, Co, and Ni) materials are superionic conductors with extremely small lithium ion migration barriers in the range from 43 to 99 meV, much lower than most oxide- and even sulfide-type cathodes. Voltage and volume calculations indicate that only $LiCrS_2$ and $LiMnS_2$ cathodes are structurally stable during cycling with the stable voltage plateaus at ∼3 V, much higher than that of the *P3m1*-$LiTiS_2$ cathode. For the first time, we studied the interfacial lithium transport resistance from a new perspective of charge transfer and redistribution at the electrode/solid-state electrolyte interface. $LiCrS_2$ and $LiMnS_2$ cathodes exhibit favorable interfacial compatibilities with Li_3PS_4 electrolyte. Our investigations demonstrate that the metallic $LiCrS_2$ and $LiMnS_2$ superionic conductors would possess excellent rate capability, high energy density, good structural stability during cycling, and favorable interfacial compatibility with Li_3PS_4 electrolyte in all-solid-state lithium ion batteries.

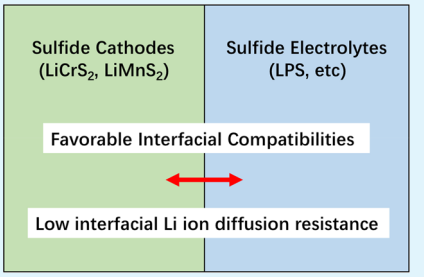

KEYWORDS: *chalcopyrite structure, electronic structure, diffusion, superionic conductor, interfacial compatibility*

INTRODUCTION

The huge demands of the large-scale energy storage system with high energy density, for applications in electric vehicles and electrical grid energy storage, raise safety concerns for the commercial rechargeable lithium ion batteries with organic liquid electrolytes, due to the instability of electrolyte and the hazard of electrolyte leakage.[1] In recent years, solid-state electrolytes (SSEs) with several natural advantages, including nontoxicity, free of leakage, high thermal stability, as well as wide electrochemical window,[2] have attracted significant attention. These advantages can potentially result in substantially enhanced safety and energy density for batteries employing SSEs in lieu of the liquid counterpart (i.e., solid-state batteries).[3]

The research of SSE materials mainly focus on the organic polymer and oxide- and sulfide-type inorganic lithium superionic conductors. Inorganic sulfide-type lithium ionic conductors are of particular interest because these materials often show higher ionic conductivities than the inorganic oxide and organic polymer and possess excellent mechanical strength, good mechanical flexibility, negligible grain-boundary resistance, and convenience of synthesizing under low temperature.[4] Among the reported sulfide-type lithium ion conductors, Li_3PS_4 (LPS)[5] and $Li_{10}GeP_2S_{12}$ (LGPS)[6] superionic conductors with high ionic conductivities comparable to that of the commercial organic liquid electrolytes are the most promising inorganic SSEs to meet the requirements of all solid-state lithium ion batteries (ASSLIBs). LPS has been regarded as one of the superionic conductors with a room temperature ionic conductivity of 1.64×10^{-4} S cm^{-1}.[7] In 2011, Kamaya et al.[8] reported another fast-ion conductor material of LGPS applied as SSE in lithium ion batteries, which exhibits an excellent lithium ion conductivity of 1.2×10^{-2} S cm^{-1} at room temperature and a very wide electrochemical window of 5 V. However, the significant difference of the electronegativity between oxygen and sulfur element makes sulfide-type SSEs show poor chemical compatibility with the high voltage oxide cathode [e.g., $LiCoO_2$ (LCO)].[9,10] For now, the electrode−electrolyte interfacial compatibility is still one of the biggest challenges for applying sulfide inorganic SSEs in ASSLIBs.[11]

People have done much research to improve the interfacial compatibility of LCO cathode−sulfide-type SSE interface, falling into two categories: coating LCO cathode and replacing oxide-type cathode with sulfide-type. Coating LCO cathode with the electron-insulating but ion-conducting oxide materials (buffer layers), such as $LiNbO_3$[12] and $Li_4Ti_5O_{12}$,[13] could

Received: July 18, 2018
Accepted: October 9, 2018
Published: October 9, 2018

Downloaded via SHANGHAI JIAO TONG UNIV on October 24, 2018 at 06:41:31 (UTC).
See https://pubs.acs.org/sharingguidelines for options on how to legitimately share published articles.

© XXXX American Chemical Society

DOI: 10.1021/acsami.8b12026
ACS Appl. Mater. Interfaces XXXX, XXX, XXX−XXX

effectively suppress the formation of a space charge layer and ease the interfacial chemical reactions and mutual diffusion,[14] dramatically decreasing the interfacial resistance of LCO−LPS interface. However, the lithium ionic conductivities at room temperature of some coating layer oxides, such as $LiNbO_3$[15] from 10^{-6} to 10^{-5} S/cm and $Li_4Ti_5O_{12}$[16] of ~10^{-7} S/cm, are much smaller than that of the LCO cathode (10^{-5}−10^{-4} S/cm)[17] and sulfide-type SSE (from 10^{-4} to 10^{-2} S/cm),[10] so developing more coating layer oxides with higher ionic conductivity is the key to further improve the electrochemical performance of ASSLIBs. On the other hand, recently, the transition-metal sulfide-type cathodes have been reexamined and widely studied to alleviate the problem of interfacial incompatibility with sulfide SSEs, which shows remarkably small interfacial resistances.[18,19] The intercalation compound titanium disulfide (*P3m1*-Li_xTiS_2) cathode with high theoretical capacity, high electronic conductivity, as well as excellent lithium diffusion exhibits high energy and power density in lithium ion batteries.[20] The ASSLIB system of TiS_2/Li_2S−P_2S_5/Li with the nanosized TiS_2 cathode demonstrates high power density over 1000 W kg^{-1} and extremely high rate capability performance.[19] The nanostructured NiS cathode in ASSLIBs exhibits excellent rate capability and cycling stability, whose reversible discharge capacities can be as high as 299 mAh g^{-1} at current densities of 500 mA g^{-1}, and reversible discharge capacities are up to 243 mAh g^{-1} after 100 cycles at current densities of 500 mA g^{-1}.[21] The layered VS_2 nanosheet cathode in ASSLIBs shows a high reversible capacity of 532.2 mAh g^{-1} at 50 mA g^{-1} after 30 cycles, and the stable discharge capacities are well-maintained at 436.8 and 270.4 mAh g^{-1} at 100 and 500 mA g^{-1} after 100 cycles, respectively.[22] Are the aforementioned transition metal sulfide cathodes best for ASSLIBs with sulfide-type SSEs? No, the lithium ion migration activation energy of them are more than 200 meV, and there may be some room to further reduce the activation energy to ~100 meV and dramatically enhance the ionic conductivity by over 2 orders of magnitude by the refined design of crystal structure.

In this work, we proposed a series of chalcopyrite-structured sulfide-type $LiMS_2$ (M = Sc, Ti, V, Cr, Mn, Fe, Co, and Ni) materials and systematically assessed their performances as cathode materials in ASSLIBs by first-principles calculation, which is a powerful tool for material research prior to experiments.[23] Some of them are mixed electron−ion conductors with both enhanced electronic and ionic conductivities compared with most reported transition metal sulfide-type cathodes. On the basis of density functional theory (DFT) calculations, we first performed phonon spectrum, elastic constant, and *ab*-initio molecular dynamics (AIMD) calculations to confirm their thermodynamic and dynamic stabilities. Then, electronic structures and activation barriers of lithium ion migration for $LiMS_2$ materials were calculated to evaluate their electronic and lithium ionic conductivities as the high-performance cathodes shall display excellent rate performances, which have been successfully applied for battery material calculations.[24,25] Voltage and volume variations during cycling of the $LiMS_2$ (M = Cr, Mn, Fe, Co, and Ni) mixed conductors were calculated to assess their energy densities and structural stabilities during cycling as cathode materials in LIBs. Lastly, the $LiMS_2$ (M = Cr and Mn) cathode−LPS electrolyte interfaces were studied to examine the interfacial compatibilities between $LiMS_2$ and sulfide SSEs from a new perspective of charge transfer and redistribution at the cathode−SSE interface for the first time. This new insight of the origin of interfacial lithium transport resistance may shed light on the rational design of ASSLIBs. Our investigations demonstrate that metallic $LiCrS_2$ and $LiMnS_2$ lithium superionic conductors would possess excellent rate performance, good structural stability during cycling, and favorable interfacial compatibility with sulfide SSEs in ASSLIBs.

COMPUTATIONAL METHODOLOGY

All atomic and electronic structure calculations were carried out by using the projector augmented wave (PAW) method in the framework of DFT,[26] as implemented in the Vienna *ab*-initio Simulation Package (VASP). The generalized gradient approximation (GGA) and Perdew−Burke−Ernzerhof (PBE) exchange functional[26] was used. Structural relaxation and electronic structure calculations were performed by using the spin-polarized GGA method.[27] Meanwhile, for more accurate descriptions of band structure and density of electron states (DOS) of $LiMS_2$, the hybrid functional of HSE06[28] was employed. After convergence tests, the plane-wave energy cutoff was set to 500 eV, and the Monkhorst−Pack method[29] with 5 × 5 × 3 and denser 11 × 11 × 5 *k*-points mesh were employed for the Brillouin zone sampling for structural relaxations and electronic structure calculations of $LiMS_2$ materials, respectively. In addition, the cathode−SSE interfacial supercell calculations used the same *k*-point mesh density as those of structural relaxations. The convergence criterions of energy and force calculations were set to 10^{-5} eV/atom and 0.01 eV $Å^{-1}$, respectively. Energy barriers of lithium ion migration were calculated based on a 2 × 2 × 1 supercell model with one lithium vacancy by the climbing image nudged elastic band (CI-NEB) method.[30] Phonon calculations were performed with 2 × 2 × 1 supercells based on the density functional perturbation theory (DFPT),[31] as implemented in the PHONOPY code.[32] In addition, *ab*-initio molecular dynamics (AIMD) simulations were performed at room temperature of 300 K in a statistical ensemble with fixed particle number, volume, and temperature (NVT) by using 2 × 2 × 1 supercells of $LiMS_2$ crystals. Time step was set to 3 fs, and supercell systems were simulated for 10000 steps, with a total time of 30 ps. A plane-wave energy cutoff of 400 eV, gamma-centered *k*-point mesh, and periodic boundary conditions were also used for AIMD simulations.

RESULTS AND DISCUSSION

Crystal Structure and Stability. Our proposed $LiMS_2$ (M = Sc, Ti, V, Cr, Mn, Fe, Co, and Ni) materials belong to the body-centered tetragonal chalcopyrite lattice structure (*I42d* group), as depicted in Figure 1a, which can be derived from the sphalerite structure (cubic *β*-ZnS structure). Double the unit cell of *β*-ZnS along the *Z* direction and then replace the eight zinc atoms with four lithium atoms and four transition metal atoms (see Figure S1). Except for the *I42d* structure, some other derivative structures (see Figure S2) at different space groups were also obtained, but we found that the *I42d* structure is the most stable configuration. Each lithium or transition metal atom in the chalcopyrite-structured $LiMS_2$ materials is bonded to four sulfur atoms forming a tetrahedron, and each sulfur atom is tetrahedrally coordinated to two lithium atoms and two transition metal atoms. Charge density plots (see Figure S3) show the M-S tetrahedral coordination is mainly covalent bonding, while Li−S tetrahedral coordination is mainly ionic bonding. The optimized lattice constants *a*, *b*, and *c* of $LiMS_2$ by DFT calculations are summarized in Table S1. The lattice constants *a* and *b* of $LiMS_2$ crystals basically decrease with the increase of atomic number of transition metals. The sulfur atom sublattice in $LiMS_2$ materials is approximately matched to a body centered cubic-like (*bcc*) anion framework (Figure 1b), minimizing the root-mean-

DOI: 10.1021/acsami.8b12026
ACS Appl. Mater. Interfaces XXXX, XXX, XXX−XXX

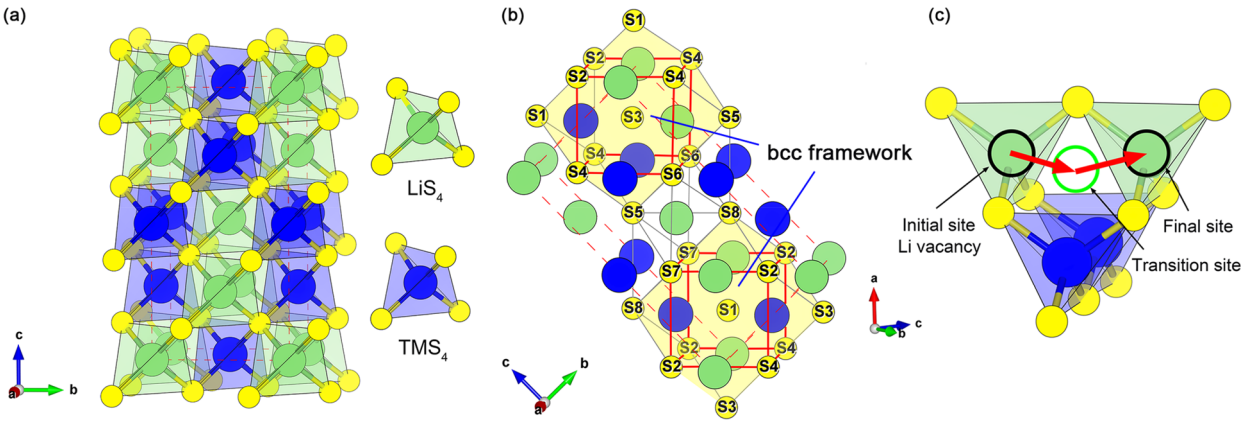

Figure 1. 3D Structural plot of (a) the unit cell of the chalcopyrite-structured $LiMS_2$ crystals, (b) body centered cubic-like (*bcc*) sulfur anion framework (S3−S2−S4−S6 and S1−S2−S4−S7) in $LiMS_2$ materials, and (c) lithium ion migration between two adjacent LiS_4 tetrahedrons. The crystal structure plots are displayed by the VESTA software.[42]

square distance for the centered lithium ion migration and eventually leading to high ionic conductivities.[33] This bcc sulfur framework is comparable with those of some reported lithium superionic conductors, such as LGPS,[8] $L_7P_3S_{11}$,[34] and $Li_{1+2x}Zn_{1-x}PS_4$.[35]

To confirm the dynamical stability of $LiMS_2$ crystals, their phonon dispersions were first calculated. All vibrational modes of our predicted $LiMS_2$ materials in Figure S4 show positive frequencies, indicating $LiMS_2$ materials are dynamically stable. Elastic constants of $LiMS_2$ (M = Sc, Ti, V, Cr, Mn, Fe, Co, and Ni) materials were calculated to verify their mechanical stabilities.[36] In accordance with the Born elastic theory,[37] elastic constant constitutes a symmetric 6 × 6 tensor matrix in the linear elastic range. Due to symmetry, the independent elastic constants are reduced to 9 values for the orthorhombic $LiMS_2$ crystals. The calculated elastic constants are summarized in Table S2. All these elastic constants well comply with the Born criteria for the mechanically stable orthorhombic crystal,[7] which are C_{ij} $(i = j) > 0$, $C_{11} + C_{22} - 2C_{12} > 0$, $C_{11} + C_{33} - 2C_{13} > 0$, $C_{22} + C_{33} - 2C_{23} > 0$, and $C_{11} + C_{22} + C_{33} + 2C_{12} + 2C_{13} + 2C_{23} > 0$, confirming the mechanical stabilities of $LiMS_2$ materials at DFT level (0 K). In addition, the elastic properties of electrode materials are crucial parameters for designing high performance LIBs.[38] Bulk modulus of crystal material is associated with elastic opposition to atomic bond stretching, and shear modulus represents resistance to plastic deformations under exterior stress. Therefore, the ratio of B/G is regarded as an important parameter measuring the dominant elasticity or plasticity of crystal material.[39] Ductile materials usually have a high B/G ratio value (more than 1.75), whereas a small value (less than 1.75) is representative of the brittle material.[40] From our elastic property calculations and comparisons in Table S1, B/G ratios of $LiMS_2$ materials are in the range from 2.29 to 7.21, suggesting that *I42d*-$LiMS_2$ materials investigated in this work shall have good ductility. Thus, when applying *I42d*-$LiMS_2$ materials as cathodes in ASSLIBs, they can achieve good mechanical contacts at the electrode−SSE interface, leading to smaller interfacial electrical resistances.

Moreover, the room temperature AIMD simulations were performed to further confirm the thermal stabilities of *I42d*-$LiMS_2$ (M = Sc, Ti, V, Cr, Mn, Fe, Co, and Ni) materials. During the whole AIMD simulation process, total potential energy of each $LiMS_2$ material vibrate around a constant, as shown in Figure S5. Crystal structures of $LiMS_2$ materials during the entire AIMD simulation processes at 300 K nearly maintain the initial tetrahedral bonding structures, although some structural deformations by thermal vibration are observed from atomic trajectories of AIMD simulations (see details in Figure S6). Further, it is found that the thermal vibration amplitudes of lithium and sulfur atoms significantly enhance with the increase of atomic number of transition metal in $LiMS_2$ materials, due to the reduction of Li−S and M−S interatomic interactions. The DFT calculated phase diagram is an effective tool for evaluating the possibility of preparing new materials.[41] Thus, we have also calculated the DFT phase diagrams of *I42d*-$LiMS_2$ materials. It is found that *I42d*-$LiMS_2$ materials are metastable in their corresponding DFT phase diagrams. But we found that partially replacing the light transition metals in $LiMS_2$ materials with heavy transition metals, such as copper and zinc, can further stabilize the tetrahedral frameworks without sacrificing much excellent lithium diffusion. Above analyses of the mechanical and thermal properties indicate these eight *I42d*-$LiMS_2$ (M = Sc, Ti, V, Cr, Mn, Fe, Co, and Ni) materials are likely to be stable or at least metastable under ambient environment.

Electronic Structure. Excellent electron transfers between electrode material and current collector and also between its redox sites are vital for high rate of electrode materials. Therefore, better understanding electronic structures of the *I42d*-$LiMS_2$ (M = Sc, Ti, V, Cr, Mn, Fe, Co, and Ni) materials is indispensable to design the sulfide-type cathodes for ASSLIBs. Herein, the spin-polarized band structures and total density of electron states (TDOS) of $LiMS_2$ materials were calculated by using the HSE06 hybrid functional, as shown in Figure 2. It can be seen that even with the same framework of crystal structure, transition metals play a critical role in the electronic structures of these eight $LiMS_2$ materials. Overall, the electronic conductivities of $LiMS_2$ materials increase with the increase of atomic number of transition metal. More interestingly, the transition from insulator, semiconductor, to conductor can be achieved by tuning transition metals in $LiMS_2$.

A closer look at the individual material shows that $LiScS_2$ exhibits completely the same electron states of the spin-up and -down channels with a large indirect band gap of 3.75 eV (Figure 2a) and hence is an insulator without spin polarization. For $LiTiS_2$ material, the electron states of the spin-up and

DOI: 10.1021/acsami.8b12026
ACS Appl. Mater. Interfaces XXXX, XXX, XXX−XXX

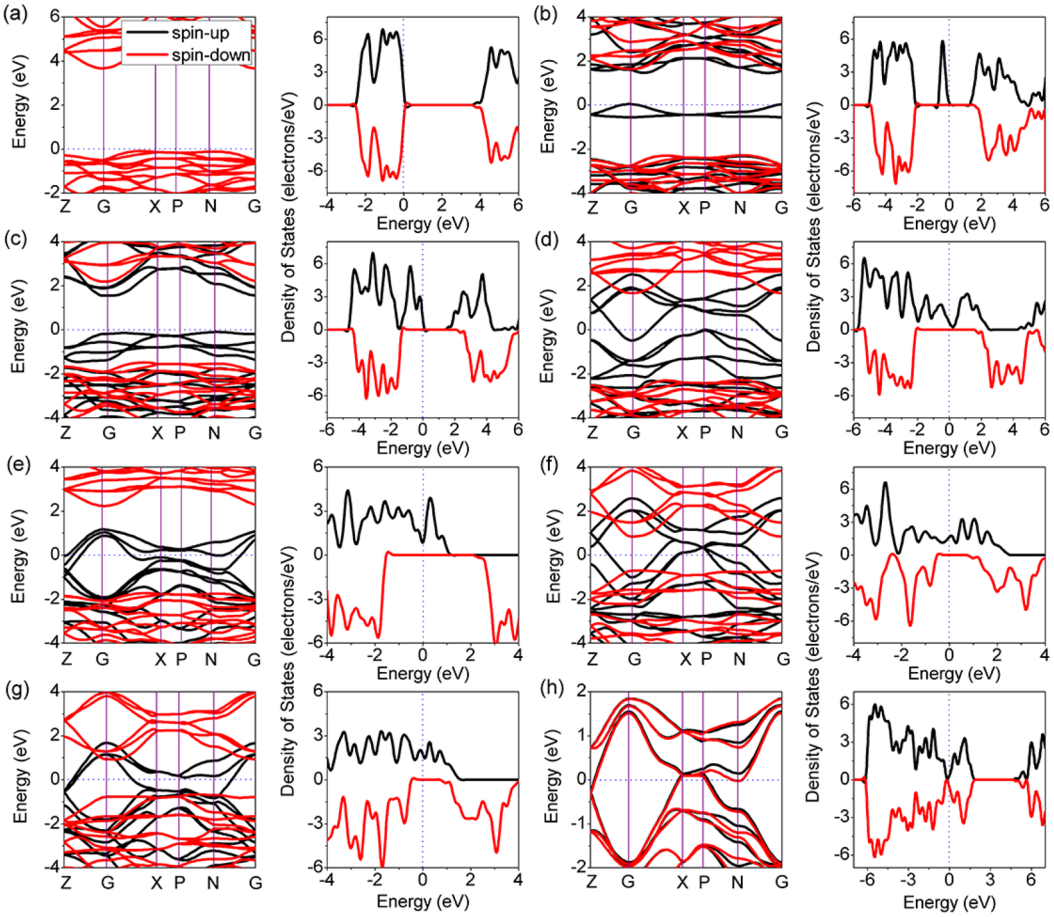

Figure 2. Band structures and spin polarized density of electron states of $LiMS_2$ materials: (a–h) for M = Sc, Ti, V, Cr, Mn, Fe, Co, and Ni, respectively. The Fermi levels are set to 0 eV.

-down channels are very different, and the band gaps of the spin-up and -down channels are 1.50 and 3.95 eV, respectively (Figure 2b). Thus, $LiTiS_2$ is a spin-polarized semiconductor. Similarly, $LiVS_2$ is also a semiconductor with a band gap of 1.48 eV and 100% spin polarization near the Fermi energy level (Figure 2c). On the basis of the poor electronic conductivity of $LiScS_2$, $LiTiS_2$, and $LiVS_2$, if their lithium ion migrations are relatively fast, they might be promising to be used as the SSE materials in ASSLIBs. In addition, $LiCrS_2$ material also shows different electronic conductivities of the spin-up and -down channels (Figure 2d). The spin-down channel shows a very large direct band gap of 4.12 eV with an insulator feature, whereas the spin-up channel exhibits metallic characteristics due to the considerable occupied electron states cross the Fermi level. Hence, $LiCrS_2$ material is intrinsically half-metallic and has 100% spin polarization near the Fermi level. Similarly, $LiMnS_2$, $LiFeS_2$, and $LiCoS_2$ materials are all intrinsically half-metallic and ferromagnetic with 100% spin polarization near the Fermi level (Figure 2, panels e, f, and g). These half-metallic $LiMS_2$ materials with high electronic conductivities are not only likely to be used as cathode materials in combination with sulfide SSEs in ASSLIBs but also applied in spintronic devices. $LiNiS_2$ is metallic without magnetism (Figure 2h) and is also promising to be used as cathode material.

Lithium Ion Migration. In rechargeable lithium ion batteries, excellent lithium ion transport in electrode is another important factor in determining good rate capability of LIBs. Lithium ion migration from one atomic site to another site in $LiMS_2$ materials is an activated process with a migration barrier. Lithium ions in $LiMS_2$ materials mainly migrate through the vacancy hopping because lithium defect chemistry (Table S3) indicates the lithium vacancy concentration is much higher than that of the lithium interstitial, and lithium vacancies dominate the defect chemistry in *I42d*-$LiMS_2$ materials. For electrode applications in LIBs, three-dimensional (3D) percolating paths with low ionic migration barriers are needed. The dimensionality of ion diffusion has important influence on the macroscopic ionic conductivity of electrode material. All lithium ion diffusion paths in $LiMS_2$ (M = Sc, Ti, V, Cr, Mn, Fe, Co, and Ni) are three-dimensional (Figure 1a). The calculated activation energy barriers of lithium vacancy migration (Figure 1c) in these eight $LiMS_2$ materials are shown in Figure 3. Surprisingly, the transition metal element also has an important effect on the activation energy barrier of Li diffusion in $LiMS_2$ materials, which significantly decreases across the 3d series of the periodic table from Sc through Ni.

For these eight ionic $LiMS_2$ (M = Sc, Ti, V, Cr, Mn, Fe, Co, and Ni) materials with the same crystal structure, the lithium ion migration is likely to be mainly affected by the Columbic interaction (ionic bond energy) between lithium cation and its adjacent sulfur anions, specifically depending on the Li–S bond length and the charge of lithium cation and sulfur anion. It is found that Li–S bond lengths in $LiMS_2$ materials are approximately the same (see Figure S7), which fall in the range from 2.47 to 2.50 Å. In addition, Bader charges of lithium ions in these eight $LiMS_2$ materials are almost the same ~0.87 *e*

DOI: 10.1021/acsami.8b12026
ACS Appl. Mater. Interfaces XXXX, XXX, XXX–XXX

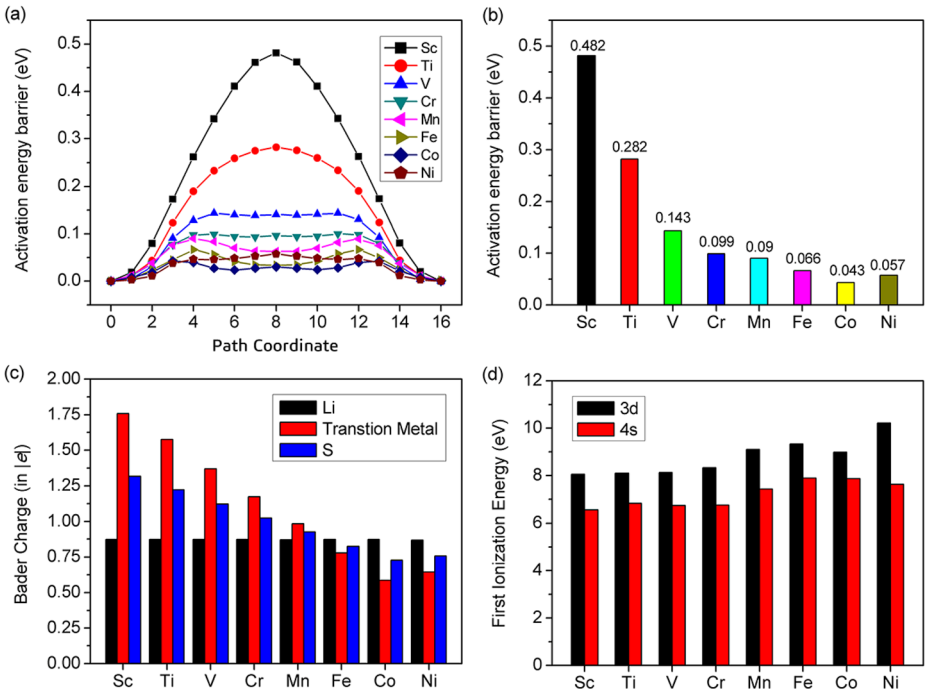

Figure 3. (a) Energy variations of lithium ion migration from one site to its adjacent vacancy in *I42d*-$LiMS_2$ (M = Sc, Ti, V, Cr, Mn, Fe, Co, and Ni) materials; (b) activation energy barriers (in eV) of lithium ion migration in $LiMS_2$; (c) Bader charges (in *e*) of each element in $LiMS_2$ (for a convenient display, the bader of S element is in the absolute value); and (d) the first ionization energies of electron in 3d and 4s orbitals for different transition metal elements.

(Figure 3c), whereas the Bader charges (absolute value) of sulfur anions become smaller with the increase of atomic number of transition metal, which is consistent with the variation trend of activation energy barrier (Figure 3b). Therefore, Bader charge of sulfur anion may be an important factor for lithium ion migration in $LiMS_2$ by varying Coulumbic interaction between Li cations and S anions. In $LiMS_2$ materials, the MS_4 tetrahedron and its adjacent LiS_4 tetrahedron are directly connected by a sulfur atom in the form of M-S-Li. Thus, the charge of sulfur anion could be contributed by its adjacent transition metal and lithium atom. Because lithium ions in these eight $LiMS_2$ materials have approximately the same charge, the electronegativity of transition metal element mainly regulates the charge difference of sulfur anion in $LiMS_2$ materials. As shown in Figure 3 (panels c and d), the variations of Bader charges of sulfur anions are in good accordance with Bader charge variations of transition metals in $LiMS_2$ materials and have strong negative correlations with the first ionization energies of electron in 3d and 4s orbitals for different transition metals. When proceeding from Sc to Ni, the electronegativity of transition metal is increasing as the 3d band fills. In other words, the smaller electronegativity difference between transition metal and sulfur, the lower the activation energy barrier for lithium migration due to the more positively charged sulfur anion and smaller Columbic interaction between sulfur anion and lithium cation.

Figure 3b shows that seven $LiMS_2$ (M = Ti, V, Cr, Mn, Fe, Co, and Ni) materials are extreme superionic conductors, except for $LiScS_2$. The activation barriers of lithium migration in these electronic conductive $LiMS_2$ (M = Cr, Mn, Fe, Co, and Ni) materials are in the range from 43 to 99 meV, superior to any known commercial $LiCoO_2$ (390 meV),[43] Li-$(Ni_xCo_yMn_z)O_2$ (357−545 meV),[44] and $LiFePO_4$ (510 meV) cathodes,[45] even *P3m1*-Li_xTiS_2 (190[46] and 200 meV[47]). These ultralow migration barriers mean that lithium ion migrations in $LiMS_2$ (M = Cr, Mn, Fe, Co, and Ni) materials are much faster than those of oxide and *P3m1*-Li_xTiS_2 cathodes. Low lithium migration barriers in these chalcopyrite-structured sulfides are likely results of the smaller electronegativity of sulfur atoms, lowering Li−S bond energy. Furthermore, the central mobilizable ion in the tetrahedron with a lower coordination number usually has super ionic conductivity than that of six- or eight-coordinated central ion; for example, the ionic conductivity of four-coordinated silver ions is much larger than that of six-coordinated silver in silver halide, such as AgF, AgCl, and AgBr.[48] Finally, the polarizable sulfur anions can deform and stabilize the transition state structures, benefiting lithium ion diffusion.

Note that these calculations of lithium migration activation barrier are based on DFT calculation at 0 K, while the atom thermal vibrations in $LiMS_2$ materials are prominent at the working temperature. Hence, the diffusion coefficients derived from the Arrhenius equation are considered to estimate the temperature-dependent transition state[49] (see details in the Supporting Information). In accordance with the transition state theory,[50] lithium ion diffusion coefficients at 300 K for these eight $LiMS_2$ (M = Sc, Ti, V, Cr, Mn, Fe, Co, and Ni) materials are calculated to be 1.35×10^{-11} cm^2/s, 2.80×10^{-8} cm^2/s, 5.96×10^{-6} cm^2/s, 3.16×10^{-5} cm^2/s, 4.60×10^{-5} cm^2/s, 1.03×10^{-4} cm^2/s, 2.58×10^{-4} cm^2/s, and 1.53×10^{-4} cm^2/s, respectively. As the atom trajectories of $LiMS_2$ supercells from AIMD simulations at 300 K in Figure S8 clearly show the ultrafast lithium diffusion ability at room temperature, it is significantly enhanced across the 3d series of the periodic table from Sc through Ni. The Nernst−Einstein equation[49] is used to obtain lithium ionic conductivity from the diffusion coefficient, and the corresponding calculated

DOI: 10.1021/acsami.8b12026
ACS Appl. Mater. Interfaces XXXX, XXX, XXX−XXX

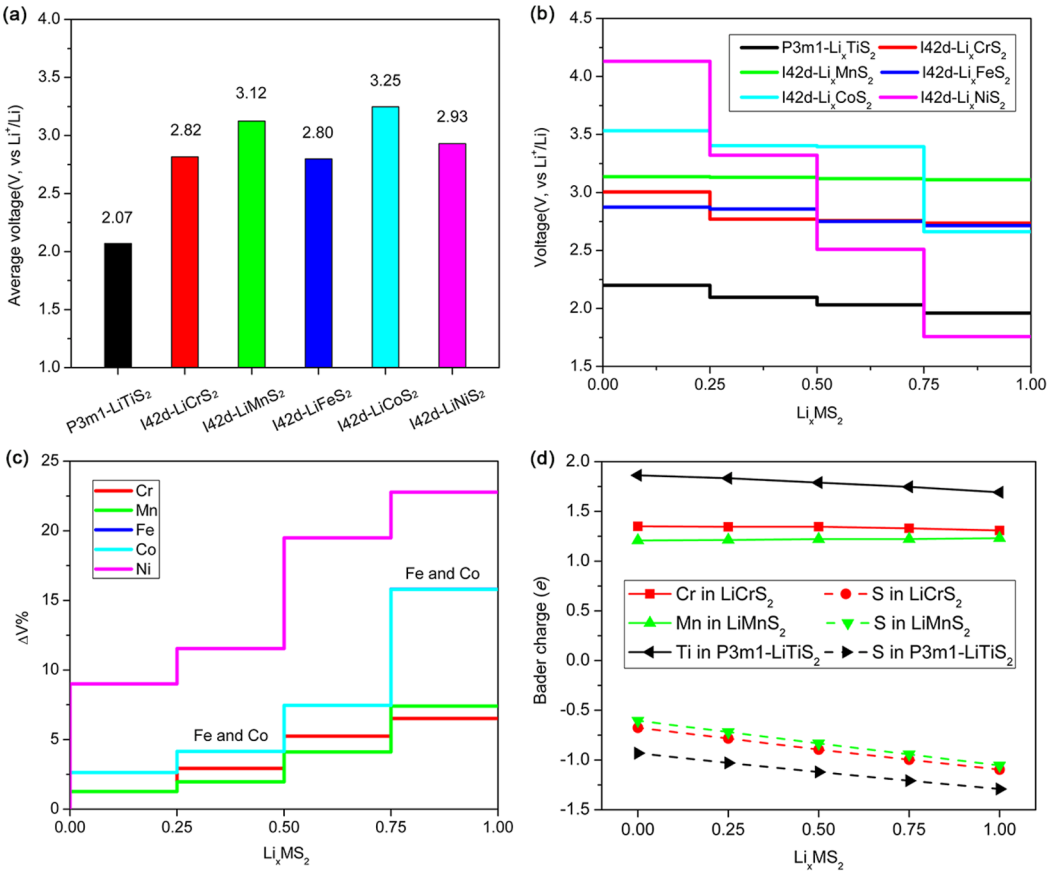

Figure 4. Calculated intercalation voltages: (a) average voltages and (b) voltage profiles against lithium metal at HSE06 level of the *P3m1*-$LiTiS_2$ and *I42d*-$LiMS_2$ (M = Cr, Mn, Fe, Co, and Ni) materials, (c) volume variations of $LiMS_2$ (M = Cr, Mn, Fe, Co, and Ni), and (d) Bader charge (in *e*) variations of transition metal and sulfur atom of $LiCrS_2$, $LiMnS_2$, and *P3m1*-$LiTiS_2$ materials during the cycling process.

values of lithium ionic conductivities at 300 K for these eight $LiMS_2$ materials are 9.03×10^{-7} S/cm, 2.01×10^{-3} S/cm, 0.45 S/cm, 2.42 S/cm, 3.47 S/cm, 8.72 S/cm, 21.80 S/cm, and 12.73 S/cm, respectively (see the details in the Supporting Information). To further benchmark our computational method, we have carefully calculated lithium ionic conductivity of LGPS with an experimental lithium migration barrier of 0.24 eV,[51] based on which its lithium ionic conductivity at 300 K was calculated to be 1.21×10^{-2} S/cm, in agreement with the experimental result of 1.2×10^{-2} S/cm,[51] validating our methodology. On the basis of ionic conductivity evaluation above, semiconducting $LiTiS_2$ and $LiVS_2$ superionic conductors can be prospectively used as SSE materials, which are comparable to 1.2×10^{-2} S/cm of the representative superionic conductor LGPS with a lithium migration barrier of 0.21−0.25 eV,[52] and these five $LiMS_2$ (M = Cr, Mn, Fe, Co, and Ni) materials with extremely excellent electronic and ionic conductivities are promising to be applied as cathodes in combination with sulfide SSEs in ASSLIBs with high-rate performance.

Voltage and Volume Variation during Cycling. High output voltage is the key to achieve high energy density of rechargeable LIBs. Thus, the theoretical intercalation voltages of $LiMS_2$ (M = Cr, Mn, Fe, Co, and Ni) mixed conductor materials were calculated by HSE06 hybridization functional method based on the basic electrochemical reaction (see the details in the Supporting Information). Generally, the HSE06 hybrid functional calculated formation energies of the transition metal oxides with localized 3d electrons are more accurate than that calculated by the standard GGA method.[53] Therefore, in this work we used the HSE06 hybrid functional to calculate the voltage and formation energy of $LiMS_2$ cathodes. However, due to the tremendous consumption of computational resource for the HSE06 calculations, we considered the unit cell with the least atoms for the intermediate delithiated compounds. There are four lithium ions in the unit cell of the fully discharged $LiMS_2$ phase, so the lithium intercalation processes of $LiMS_2$ cathodes were divided into four stages with three intermediate delithiated compounds and one fully delithiated compound, including $Li_{0.75}MS_2$, $Li_{0.5}MS_2$, $Li_{0.25}MS_2$, and MS_2, as shown in Figure S9. Then, we got the DFT-calculated formation energies (with HSE06 hybrid functional) of the intermediate delithiated compounds of Li_xMS_2 (M = Cr, Mn, Fe, Co, and Ni) materials, as shown in Figure S10a. The HSE06 formation energies for each of the intermediate delithiated compounds Li_xMS_2 (M = Cr, Fe, Co, and Ni) cathode materials are negative, indicating during the charge−discharge processes the solid-solution reaction mechanism is likely to happen for Li_xMS_2 (M = Cr, Fe, Co, and Ni) cathodes. On the other hand, the HSE06 formation energies of the Li_xMnS_2 intermediate delithiated compounds are positive, indicating the intermediate delithiated Li_xMnS_2 compound is likely to decompose to the fully discharged $LiMnS_2$ and fully charged MnS_2 phases, which is similar to the case of $LiFePO_4$.[54] However, we note that limited configurations were considered within HSE calculations and more complicated Li configurations using larger supercells may further reduce the formation energies, which seems especially

DOI: 10.1021/acsami.8b12026
ACS Appl. Mater. Interfaces XXXX, XXX, XXX−XXX

important for $LiMnS_2$ to determine whether it will adopt two-phase reaction during charge and discharge. Thus, we determined the GGA formation energy for intermediate delithiated Li_xMnS_2 with larger supercells and more complex configurations in Figure S10b, which turns out to be positive still. Therefore, we expect that $LiMnS_2$ cathode material obeys the two-phase reaction mechanism like $LiFePO_4$, which has been proved to be a mixture of the Fe^{3+}/Fe^{2+} mixed-valent intermediate $Li_{0.05}FePO_4$ and $Li_{0.89}FePO_4$ phases with the same olivine group (*Pnma*).[55]

The calculated average intercalation voltage and voltage profiles corresponding to each lithium intercalation/extraction stage are depicted in Figure 4 (panels a and b, respectively). We have also calculated the average intercalation voltage and voltage profiles of *P3m1*-$LiTiS_2$ cathode. It can be seen from Figure 4a that our calculated average intercalation voltage of 2.07 V for *P3m1*-$LiTiS_2$ cathode is in good accordance with the reported experimental and theoretical results of ∼2.1 V,[18,19,47] indicating the accuracy and rationality of our calculation methods of voltage based on the HSE06 hybrid functional. The average intercalation voltages of $LiMS_2$ (M = Ti, V, Cr, Mn, Fe, Co, and Ni) materials fall in the range from 2.80 to 3.25 V, which are smaller than those of the corresponding oxide cathodes, such as $LiCoO_2$ and $LiNi_xCo_yMn_zO_2$, but are about 1.5 times that of *P3m1*-$LiTiS_2$ cathode (2.1 V). We believe that the electrochemical potential of $LiMS_2$ materials can be further enhanced by element substitutions, which are similar to those cases of cation doping in oxide cathode materials.[56] Voltage profiles in Figure 4b show that $LiMnS_2$ cathode shows very long voltage plateaus around 3 V during the whole lithium insertion/extraction process, and it is a typical feature of the two-phase reaction mechanism, which is consistent with the positive formation energies of the Li_xMnS_2 intermediate delithiated compounds. For $LiMS_2$ (M = Cr, Fe, and Co) cathode materials, all their voltage curves show both plateaus and significant drops, and they may obey the two-phase reaction and solid-solution reaction mechanism at the different charge−discharge stages. In addition, $LiNiS_2$ cathode material has significantly large voltage drops at different lithium intercalation/extraction stages, and its voltage sharply reduces from 4.18 to 1.75 V upon lithium extraction. Thus, $LiNiS_2$ cathode is much likely to fully obey the solid-solution reaction mechanism. It is of interest to note that when much more intermediate delithiated compounds are considered, the voltage plateaus will shorten and voltage profiles of cathodes obeying the solid-solution mechanism will get steeper, especially for $LiNiS_2$. Therefore, some calculated voltage plateaus of the Li_xMS_2 (M = Ti, Cr, Fe, Co, and Ni) cathode materials can not completely represent the typical feature of the two-phase reaction, and it is just related to the relatively unfavorable formation energies (negative but close to zero) of the intermediate delithiated compounds (Figure S10a).

The minor structural variations upon lithium insertion/extraction are beneficial for maintaining good cycling stability. In this work, we calculated the crystal volume differences between the different delithiated configurations to evaluate their structural variations of $LiMS_2$ (M = Cr, Mn, Fe, Co, and Ni) cathode materials during the whole charge−discharge processes, as shown in Figure 4c. The maximum volume expansion rates of $LiCrS_2$ and $LiMnS_2$ materials during the whole lithium insertion/extraction process are 6.5% and 7.5%, respectively, smaller than ∼10% of the *P3m1*-$LiTiS_2$ cathode.[57,58] These volume variations of 6.5−7.5% are acceptable, due to the good mechanical flexibility (softness) of $LiMS_2$ sulfides (see the Bulk modulus, Young's modulus, and Shear modulus in Table S1). In addition, the TMS_4 tetrahedral structures of the intermediate delithiated and fully delithiated compounds are well-preserved. However, the maximum volume expansion rates of $LiMS_2$ (M = Fe, Co, and Ni) materials are 16%, 16%, and 22.6%, respectively, resulting in structural pulverization and electrical disconnection between active materials and current collector and finally fast capacity fading. In accordance with the partial densities of states (PDOS) of $LiMS_2$ (M = Cr, Mn, Fe, Co, and Ni) materials in Figure S11, the S atom participates in redox reactions along with transition metal atoms because of the abundant 3p electron states near Fermi level, and S atoms in *P3m1*-$LiTiS_2$ show the same behaviors (Figure S11f). To further figure out the element redox reactions of the most promising $LiCrS_2$ and $LiMnS_2$ cathode during cycling, Bader charge variations of the transition metal and sulfur atom in the intermediate delithiated and fully delithiated compounds were calculated, as shown in Figure 4d. During the whole cycling process, charge variation of sulfur atoms is more remarkable than that of transition metal, both for $LiCrS_2$ and $LiMnS_2$, indicating S atoms actively participate in the redox reactions and contribute to voltage output during cycling, which is highly consistent with that of *P3m1*-$LiTiS_2$ cathode materials. Hence, S atoms in $LiMS_2$ will be inevitably oxidized to the S elementary substance at the end of the charge. Different from the oxygen gas release of the full-charged $LiCoO_2$ cathode, the formed solid-state sulfur does not escape from the sulfide cathodes. In addition, the stabilities of the fully charged CrS_2 and MnS_2 compounds are further confirmed by 300 K AIMD simulations and phonon spectra (see the details in Figure S12). Thus, sulfide cathode materials would be structurally stable and have better reversibility.

Moreover, the ionic and electronic conductivities for a cathode material will be significantly affected by the state of charge during cycling. Besides the key factor of Li−S attractive electrostatic interaction, Li diffusion in cathodes at different charge states during cycling is also affected by the Li−Li repulsive electrostatic interactions. The previous work indicates that the Li diffusion energy barrier of the fully discharged phase is usually to be a maximum, and it decreases with more Li delithiated from cathodes during the charging process.[50,59] In this work, we only calculated the Li diffusion energy barrier of the fully discharged $LiMS_2$ phases, which can be lowered in the intermediate delithiated compounds of Li_xMS_2 due to the reduced Li−Li repulsive and Li−S attractive electrostatic interaction (Figure 4d). Therefore, the excellent ion diffusion of the fully discharged $LiMS_2$ phase is sufficient to evaluate whether Li_xMS_2 cathodes will show the good ionic conductivities during the whole charge−discharge processes. Furthermore, we have calculated the TDOS of the intermediate delithiated compounds of the metallic Li_xMS_2 materials (M = Cr, Mn, Fe, Co, and Ni, where x = 0, 0.25, 0.5, 0.75, and 1.0), as shown in Figure S13. They show the metallic characteristics of the charged Li_xMS_2 phases are fully maintained during the continual delithiation process, indicating that the $LiMS_2$ (M = Cr, Mn, Fe, Co, and Ni) cathodes also exhibit excellent electronic conductivities during the whole charge−discharge processes. With this, we expect that both the metallic $LiCrS_2$ and $LiMnS_2$ superionic conductors are promising to be used as cathode materials, constituting

DOI: 10.1021/acsami.8b12026
ACS Appl. Mater. Interfaces XXXX, XXX, XXX−XXX

ASSLIBs along with sulfide SSEs to obtain higher rate and better cycling stability than the *P3m1*-$LiTiS_2$ cathode.

Interfacial Compatibility with Li_3PS_4 Electrolyte. Experiments have verified that LPS electrolyte shows poor chemical compatibility against the high voltage LCO cathode with a high interfacial ion transport resistance.[10,60] On one hand, it is because the large difference of the lithium chemical potentials between the sulfide SSE and oxide electrode makes lithium ions at the electrolyte side badly depleted, causing the significant decrease of the interstitial lithium ion carriers at the sulfide SSE side.[61,62] On the other hand, the interfacial layer with 10 nm thickness and the mutual diffusions of Co and S during cycling was observed between LCO cathode and $Li_2S-P_2S_5$ electrolyte by the transmission electron microscopy (TEM) and energy dispersive X-ray spectroscopy technology, and the interfacial degradations caused by the chemical or electrochemical reactions are inferred as another reason for the large interfacial resistance at the cathode−SSE interface.[63]

In this work, we chose β-LPS superionic conductor (with much higher ionic conductivity than γ-LPS[5]) to construct the $LiMS_2$ (M = Cr and Mn) cathodes−LPS electrolyte interfaces and examined their interfacial compatibilities. Many experimental electrochemical impedance spectroscopies show the interfacial resistance of the sulfide cathode/sulfide SSE system is significantly smaller than that of the oxide-type cathode/sulfide SSE.[12,22,60,64] Moreover, both the element mutual diffusion of Cr ↔ P and Mn ↔ P at $LiCrS_2$−LPS and $LiMnS_2$−LPS interface, respectively, are thermodynamically unfavorable with very positive element exchange energies of 2.59 and 1.37 eV, respectively, suggesting the structural degradations originating from the mutual diffusion of elements and chemical reaction at the interface are much gentler than that of the LCO/LPS case with negative Co ↔ P exchange energies in the range of −3.80 ∼ −2.80 eV and favorable Co ↔ P mutual diffusions at the interface. Therefore, our calculation models for the sulfide-type cathode−SSE interface do not consider the weak interfacial chemical and electrochemical reactions. LGPS is another important sulfide-type SSE, but considering the unit cell of LGPS has 40 atoms, the interface calculations based on the supercell structure of LGPS will be a challenge and hence are not considered in this work.

To build reasonable and stable interface structures, we should have abundant knowledge of the surface properties of $LiMS_2$ and LPS materials. Surface energies of $LiCrS_2$ material with different crystallographic planes and atom terminations were calculated, as summarized in Table S4, indicating the Li- and Cr-terminated (112) [top] and S-terminated $(\overline{112})$ [bottom] surface of the chalcopyrite-structured $LiCrS_2$ material (see details in Figure S14a) is the most stable one. Furthermore, the (112) surface of $LiCrS_2$ material is polar due to the asymmetric surface atomic structure. Similarly, the cation-terminated (112) surface of the Kesterite material Cu_2ZnSnS_4 is most stable,[65] which shows a preferential growth orientation of (112) in experiments.[66] Therefore, we expect that the chalcopyrite-structured $LiMnS_2$ also exhibits the similar surface properties. Although the favorable stability of the (100) surface of β-LPS is suggested by the previous theoretical study,[67] experimental observations still demonstrate the appearance of (010) surface in its particles,[68] and it provides important lithium ion migration channels along the [010] direction.[7,67] Therefore, in this work, the Li- and S-terminated LPS (010) surface (see details in Figure S14b) is selected to construct the cathode−SSE interface systems, which is consistent with the practices in the previous computational work of the LCO (110)−LPS (010) interface.[9,14] Because the (112) surfaces of $LiCrS_2$ and $LiMnS_2$ materials are polarized with different surface terminations, both the Li- and Cr (Mn)-terminated (112) surface and S-terminated $(\overline{112})$ surface are considered for cathode−SSE interface calculations. Eventually, the asymmetric sulfide-type cathode/SSE/cathode interface systems are constructed with supercell lattice mismatches less than 6.45% (see details in Table S5), as shown in Figure S15a, which are S-terminated $LiCrS_2$ (112) cathode/LPS (010) electrolyte/Li- and Cr-terminated $LiCrS_2$ (112) cathode and S-terminated $LiMnS_2$ (112) cathode/LPS (010) electrolyte/Li- and Mn-terminated $LiMnS_2$ (112) cathode, hereafter denoted as LCS/LPS and LMS/LPS, respectively. Moreover, a representative LCO (110) cathode/LPS (010) electrolyte interface is also calculated for the convenience of making comparisons with our sulfide cathodes (see the details in Figure S15b).

To meet the requirements of good compatibility of the electrode−SSE interface for high rate capability and cycling stability performance in ASSLIBs, the stable interfacial structure with small distortion, as thin as interfacial layer, and low lithium ion transport resistance are all desired. Both interface energies of LCS−LPS and LMS−LPS systems are negative, which are −0.14 and −0.04 eV/Å^2, respectively. Figure S16 shows both the optimized LCS−LPS and LMS−LPS interface structures with small interfacial atom distortions, at which no highly Li concentrated layer is formed, likely to reduce the interfacial resistance for Li ion diffusions.[9,61] While for the optimized LCO−LPS interface in Figure S17, the interfacial Li atoms are significantly adsorbed from LPS electrolyte side to LCO surface side due to the large difference of electronegativity between oxygen and sulfur, which is consistent with the reported computational work.[9] Thus, a highly Li concentrated layer is formed at the LCO side, correspondingly making Li at LPS side depleted, which is in strong contrast to those LCS−LPS and LMS−LPS interfaces without highly Li concentrated layer, and contribute to the high interfacial lithium transport resistance.[9,61] When combining with sulfide SSE, LCS and LMS sulfide cathodes can produce smaller interface structural deformation than LCO oxide cathode, and they may be more compatible with sulfide SSE and possess smaller resistances for Li diffusion.

Except for the effect of the interfacial Li concentrated layer and interfacial degradations, the charge transfer and redistribution among the interfacial atoms also affect the lithium ion transport across the interface, because lithium ion migration is greatly affected by the Columbic interactions. Furthermore, the interfacial electronic structure properties control the electron transport processes at interfaces.[69] When a metallic electrode contacting with a semiconducting SSE, charges in the interfacial area will be redistributed. Therefore, it is necessary to study the interfacial electron transport of these cathode−SSE interfacial systems. First, the planar averaged electrostatic potentials normal to the interface were calculated, which are the driving forces of electron transfer and determine the transfer direction of electrons.[70] The choice of the exchange correlation functional in DFT calculations has little impact on the electrostatic potential, so we continued to use the conventional PBE functional to calculate the planar-averaged electrostatic potentials of the cathode−SSE interfaces. Figure 5 (panels a and b) shows the calculated planar and macroscopic average electrostatic potential curves of the optimized LCS−

DOI: 10.1021/acsami.8b12026
ACS Appl. Mater. Interfaces XXXX, XXX, XXX−XXX

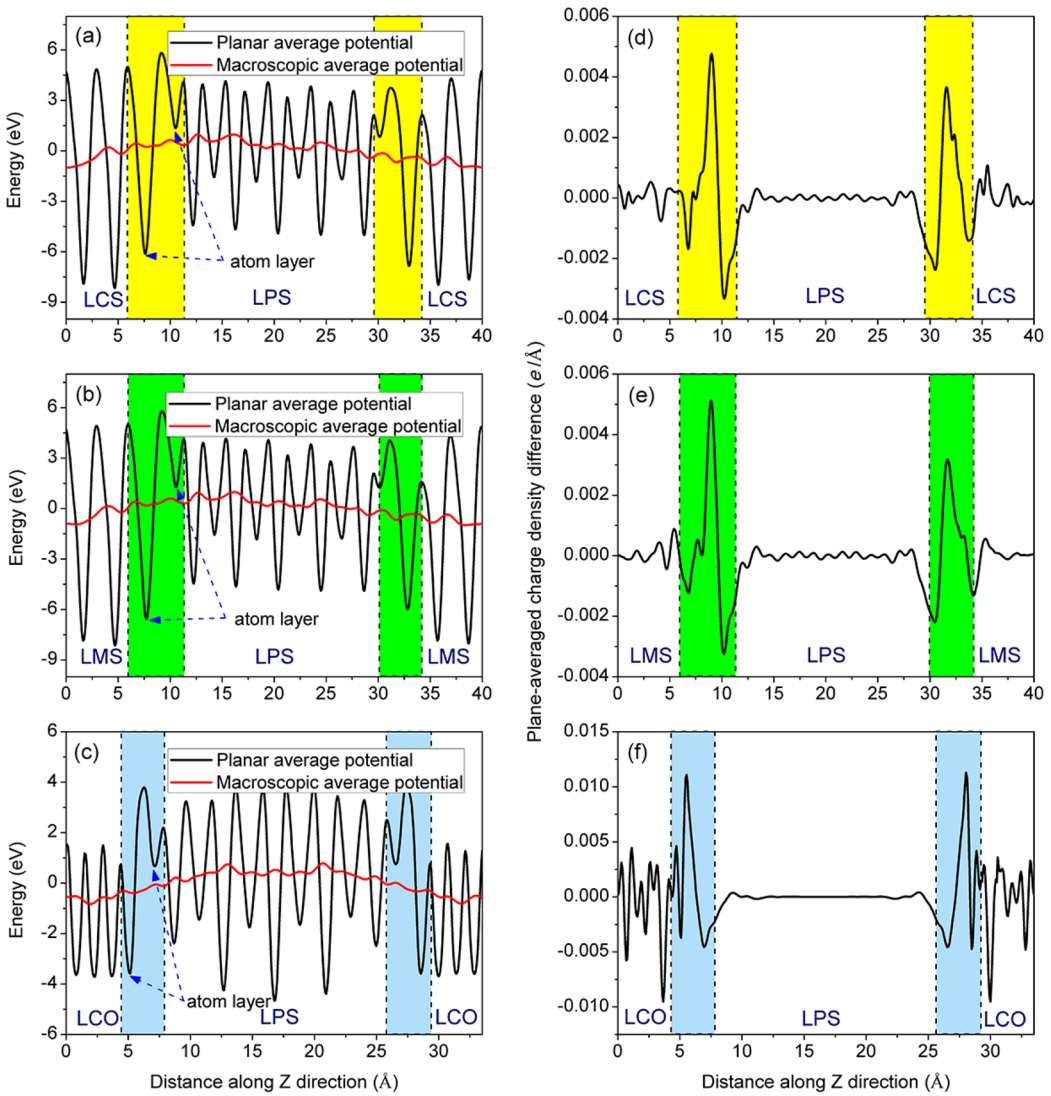

Figure 5. Planar (x−y) and macroscopic averaged electrostatic potential curves along the *Z* direction of the optimized (a) LCS−LPS, (b) LMS−LPS, and (c) LCO−LPS interfaces; planar-average charge density differences along the *Z* direction of the optimized (d) LCS−LPS, (e) LMS−LPS, and (f) LCO−LPS interfaces, where positive and negative values represent electron gain and loss, respectively. The colorful dotted line boxes represent the interface area (two atoms thick) with remarkable atom structure deformations and charge redistributions.

LPS and LMS−LPS interfaces, respectively. The planar average electrostatic potential curves oscillate within the entire supercell structure, and each valley of them can be treated as the approximated position of an atomic layer. Both for the metal atom-terminated LCS or LMS cathode−LPS electrolyte interface area (two atoms thick, the right dotted line box) and S-terminated LCS or LMS cathode−LPS electrolyte interface area (two atoms thick, the left dotted line box), there are significant macroscopic average electrostatic potential droppings from the LPS electrolyte side to the LCS or LMS cathode side at the interfacial region, driving electrons transferring from the LPS electrolyte to the LCS or LMS cathode, increasing the hole concentration in LPS electrolyte surface and the electron concentration in LCS and LMS cathode surfaces. While for the oxide-type LCO−LPS interface in Figure 5c, the same macroscopic average electrostatic potential droppings from the LPS electrolyte side to the LCO cathode side are also observed, which impel electrons transferring from LPS electrolyte to LCO cathode. To further figure out electron transfer and redistributions at the interface, the charge density differences between the cathode−SSE two phases and atomic Bader charges were calculated based on the fully optimized interface structures. Figure 5 (panels d and e) shows the planar-average charge density differences of the optimized LCS−LPS and LMS−LPS interfaces, respectively, and the calculated Bader charges of the interfacial S atoms of LCS−LPS and LMS−LPS interfaces are listed in Table S6 and S7, respectively. They clearly depict that when the LPS electrolyte (010) surface contacts the LCS or LMS (112) cathode surface, electron transfer and redistribution will occur with the interfacial S atoms in the LPS electrolyte surface losing some electrons and the interfacial S atoms in LCS or LMS cathodes surface gaining some electrons, which are in good accordance with the macroscopic average electrostatic potential results in Figure 5 (panels a and b).

To better understand the lithium diffusions across the LMS-LPS, LCS-LPS and LCO-LPS interfaces, we performed NEB calculations for the three interface models with only the diffusion lithium atom allowed to be relaxed. Thus the calculated absolute values of lithium migration barriers within

DOI: 10.1021/acsami.8b12026
ACS Appl. Mater. Interfaces XXXX, XXX, XXX−XXX

the interface NEB calculations are not accurate but the variation trends of the lithium diffusion barriers across the interaces are meaningful. Interestingly, we find out that electron transfer and redistribution at the LCS−LPS and LMS−LPS interfaces do not harm the interfacial lithium ion transport. The activation energy barriers for lithium diffusing from the cathode bulk to the electrolyte bulk through the interface area, as shown in Figure S18, show for the LCS−LPS interface the energy barrier of lithium ion diffusion along path1 (Figure S18b) in LCS cathode is 120 meV (Figure S18a), which is basically consistent with the calculated value of 99 meV of its bulk in the foregoing Part3.3, while path2 in the LCS cathode surface shows a high energy barrier of 310 meV, much larger than that of its bulk. For path3 and path4, we find their energy barriers are lower than that of the bulk (path5). Therefore, lithium ions diffuse across the LCS−LPS interface and need to overcome an energy barrier of 680 meV (path2-path3-path4), and the main restriction factor is the lithium migration in LPS electrolyte surface (path3 and path4). Because the tremendous consumption of computational resource for the interface NEB calculations, the lithium diffusion barrier calculations for LMS−LPS are not performed. But we expect that lithium ion diffusion across the LMS−LPS interface should show behaviors with similar results as those of the LCS−LPS interface. Therefore, LCS−LPS and LMS−LPS interfaces have good compatibility, enabling high rate capability and cycling stability in ASSLIBs.

Similarly, when the LPS electrolyte (010) surface contacts with the LCO (110) surface to form the LCO−LPS interface, the interfacial S atoms in the LPS electrolyte mainly loses electrons and the interfacial O atoms in LCO cathode surface gain electrons, as shown in Figure 5e and Tables S8 and S9. However, the electron transfer and redistribution at the LCO−LPS interface further harms the interfacial lithium ion transport. The increase of the negative charge of the interfacial O atoms in the LCO cathode (see details in Table S9) enhance the Coulumbic interaction between the lithium cation and its adjacent oxygen anions, which eventually increases the interfacial lithium transport resistance. The LCO−LPS interface NEB calculations indicate the lithium diffusion energy barrier in LCO surface (path2 in Figure S18c) is higher than that of its bulk (path1), and is also much higher than that of lithium diffusion in the LPS surface (path3). Moreover, the energy barriers of lithium ion diffusion along path3 and path4 in the LPS surface are lower than that of the bulk (path5). Therefore, lithium ions diffusing across the LCO−LPS interface should overcome a very high energy barrier of 1.3 eV (path2-path3-path4), and the main restriction factor is lithium migration in the LCO cathode surface (path2). Although we note the calculated absolute values of the interfacial lithium diffusion energy barriers may not be accurate, the variations of the lithium ion diffusion energy barrier for the LCS−LPS and LCO−LPS interfaces are consistent with the foregoing analysis of the interfacial electron transfer and redistributionand convincingly support the new perspective of charge transfer and redistribution at the electrode−SSE interface, affecting the interfacial lithium ion transport resistance. Moreover, the planar-average charge density difference of the LCO−LPS interface in Figure 5f demonstrates that much inner atoms of LCO cathode also take part in the interfacial charge transfer and redistributions, causing the greater interfacial space charge layer and thicker interface layer. It should be noted that the direct experimental measurements of charge transfer and redistribution at the electrode−SSE tiny interface area have not been done yet. Moreover, the cause of the experimentally macroscopic interfacial resistance between SSE and cathode is very complicated and interlaced by multifactors, such as space charge layer, interfacial structural disorders induced by the interfacial chemical reaction or element mutual diffusion, and lattice mismatch during cycling.[9] However, the charge transfer and redistribution at the electrode−SSE interface affecting the interfacial lithium transport is a universal physics, and it provides another important point of view for understanding the origin of interfacial resistance in ASSLIBs, along with the perspective of interfacial structure disorder and space charge layer theory.[9,61]

CONCLUSION

On the basis of density functional theory calculations, the electrochemical properties and interfacial compatibility with sulfide SSEs of the chalcopyrite structured $LiMS_2$ (M = Sc, Ti, V, Cr, Mn, Fe, Co, and Ni) materials were theoretically assessed, aiming to lessen the interface problem in all-solid-state lithium ion batteries, especially due to the incompatibility between oxide cathode and sulfide SSE. Phonon spectrum, elastic constant, *ab*-initio molecular dynamics simulations, and DFT calculated phase diagram indicate these eight $LiMS_2$ materials are metastable at room temperature. Four $LiMS_2$ (M= Cr, Mn, Fe, and Co) materials are half-metallic with 100% spin polarization near the Fermi level, which can be applied in spintronic devices. $LiMS_2$ (M = Cr, Mn, Fe, Co, and Ni) materials are superionic conductors with extremely small migration barriers in the range from 43 to 99 meV, which are much lower than those of oxide cathodes. Voltage and volume calculations indicate that $LiCrS_2$ and $LiMnS_2$ cathodes are structurally stable during cycling with stable voltage platforms around 3 V, much better than that of *P3m1*-$LiTiS_2$ cathode. Li- and Cr (Mn)-terminated (112) [top] and S-terminated ($\overline{112}$) [bottom] surface is the most stable surface of $LiCrS_2$ and $LiMnS_2$ materials. To the best of our knowledge, it is the first time for the interfacial resistance to be studied from a new perspective of the charge transfer and redistribution at the electrode−SSE interface. Electrons can transfer from Li_3PS_4 electrolyte to $LiCrS_2$ or $LiMnS_2$ electrode of the $LiCrS_2$ or $LiMnS_2$−Li_3PS_4 interface system, reducing lithium migration resistance across the interface. $LiCrS_2$ and $LiMnS_2$ cathodes exhibit more favorable interfacial compatibility with Li_3PS_4 electrolyte than $LiCoO_2$ oxide cathode. This new insight of charge transfer and redistribution at the electrode−SSE interface affecting interfacial lithium ion transport provides another important point of view for better understanding the origin of interfacial resistance in all-solid-state lithium ion batteries. Our investigations demonstrate that the metallic $LiCrS_2$ and $LiMnS_2$ superionic conductors would possess extremely excellent rate, good structural stability during cycling, and favorable interfacial compatibility with sulfide SSEs in all-solid-state lithium ion batteries.

ASSOCIATED CONTENT

Supporting Information

The Supporting Information is available free of charge on the ACS Publications website at DOI: 10.1021/acsami.8b12026.

Diagram of evolution process of *I42d*-$LiMS_2$; lattice parameters and elastic constants of $LiMS_2$; charge

DOI: 10.1021/acsami.8b12026
ACS Appl. Mater. Interfaces XXXX, XXX, XXX−XXX

densities and phonon dispersions; potential energy fluctuations of AIMD simulation; atomic trajectories of $LiMS_2$ AIMD simulations with and without vacancy defects; lithium defect chemistry; Li−S bond lengths; lithium ion diffusion coefficient and ionic conductivity; structural plots, DFT calculated formation energies, and TDOS of the intermediate delithiated and fully delithiated compounds; voltage calculation; AIMD simulation atomic trajectories and phonon spectra the fully delithiated CrS_2 and MnS_2 compounds; surface energies of $LiCrS_2$; lattice constants of cathode/electrolyte interface; structural plots of cathode/electrolyte/cathode interface; energy variations of lithium migration from cathode to electrolyte; and Bader charge of sulfur atoms in the cathode/electrolyte interface (PDF)

AUTHOR INFORMATION

Corresponding Author

*E-mail: hong.zhu@sjtu.edu.cn.

ORCID

Hong Zhu: 0000-0001-7919-5661

Notes

The authors declare no competing financial interest.

ACKNOWLEDGMENTS

H. Z acknowledges funding supports from the National Natural Science Foundation of China (51602196) and the Shanghai Sailing Program (16YF1406000). S.-H. Bo ackonwledges funding support from Shanghai Sailing Program (18YF1411100). All simulations were performed at the Shanghai Jiao Tong University High Performance Computing Center.

REFERENCES

(1) Manthiram, A.; Yu, X.; Wang, S. Lithium Battery Chemistries Enabled by Solid-State Electrolytes. *Nat. Rev. Mater.* **2017**, *2*, 16103.

(2) Deng, Z.; Zhu, Z.; Chu, I.-H.; Ong, S. P. Data-Driven First-Principles Methods for the Study and Design of Alkali Superionic Conductors. *Chem. Mater.* **2017**, *29*, 281−288.

(3) Bachman, J. C.; Muy, S.; Grimaud, A.; Chang, H. H.; Pour, N.; Lux, S. F.; Paschos, O.; Maglia, F.; Lupart, S.; Lamp, P.; Giordano, L.; Shao-Horn, Y. Inorganic Solid-State Electrolytes for Lithium Batteries: Mechanisms and Properties Governing Ion Conduction. *Chem. Rev.* **2016**, *116*, 140−162.

(4) Tatsumisago, M.; Nagao, M.; Hayashi, A. Recent Development of Sulfide Solid Electrolytes and Interfacial Modification for All-Solid-State Rechargeable Lithium Batteries. *J. Asian. Ceram. Soc.* **2013**, *1*, 17−25.

(5) Homma, K.; Yonemura, M.; Kobayashi, T.; Nagao, M.; Hirayama, M.; Kanno, R. Crystal Structure and Phase Transitions of the Lithium Ionic Conductor Li_3PS_4. *Solid State Ionics* **2011**, *182*, 53−58.

(6) Du, F.; Ren, X.; Yang, J.; Liu, J.; Zhang, W. Structures, Thermodynamics, and Li^+ Mobility of $Li_{10}GeP_2S_{12}$: A First-principles Analysis. *J. Phys. Chem. C* **2014**, *118*, 10590−10595.

(7) Yang, Y.; Wu, Q.; Cui, Y.; Chen, Y.; Shi, S.; Wang, R. Z.; Yan, H. Elastic Properties, Defect Thermodynamics, Electrochemical Window, Phase Stability, and Li(+) Mobility of Li_3PS_4: Insights from First-Principles Calculations. *ACS Appl. Mater. Interfaces* **2016**, *8*, 25229−25242.

(8) Kamaya, N.; Homma, K.; Yamakawa, Y.; Hirayama, M.; Kanno, R.; Yonemura, M.; Kamiyama, T.; Kato, Y.; Hama, S.; Kawamoto, K.; Mitsui, A. A Lithium Superionic Conductor. *Nat. Mater.* **2011**, *10*, 682−686.

(9) Haruyama, J.; Sodeyama, K.; Han, L.; Takada, K.; Tateyama, Y. Space−Charge Layer Effect at Interface between Oxide Cathode and Sulfide Electrolyte in All-Solid-State Lithium-Ion Battery. *Chem. Mater.* **2014**, *26*, 4248−4255.

(10) Kato, Y.; Hori, S.; Saito, T.; Suzuki, K.; Hirayama, M.; Mitsui, A.; Yonemura, M.; Iba, H.; Kanno, R. High-Power All-Solid-State Batteries Using Sulfide Superionic Conductors. *Nat. Energy.* **2016**, *1*, 16030.

(11) Zhu, Y.; He, X.; Mo, Y. First Principles Study on Electrochemical and Chemical Stability of Solid Electrolyte−Electrode Interfaces in All-Solid-State Li-ion Batteries. *J. Mater. Chem. A* **2016**, *4*, 3253−3266.

(12) Ohta, N.; Takada, K.; Sakaguchi, I.; Zhang, L.; Ma, R.; Fukuda, K.; Osada, M.; Sasaki, T. $LiNbO_3$-Coated $LiCoO_2$ as Cathode Material for All Solid-State Lithium Secondary Batteries. *Electrochem. Commun.* **2007**, *9*, 1486−1490.

(13) Ohta, N.; Takada, K.; Zhang, L.; Ma, R.; Osada, M.; Sasaki, T. Enhancement of the High-Rate Capability of Solid-State Lithium Batteries by Nanoscale Interfacial Modification. *Adv. Mater.* **2006**, *18*, 2226−2229.

(14) Haruyama, J.; Sodeyama, K.; Tateyama, Y. Cation Mixing Properties toward Co Diffusion at the $LiCoO_2$ Cathode/Sulfide Electrolyte Interface in a Solid-State Battery. *ACS Appl. Mater. Interfaces* **2017**, *9*, 286−292.

(15) Glass, A. M.; Nassau, K.; Negran, T. J. Ionic Conductivity of Quenched Alkali Niobate and Tantalate Glasses. *J. Appl. Phys.* **1978**, *49*, 4808−4811.

(16) Wilkening, M.; Amade, R.; Iwaniak, W.; Heitjans, P. Ultraslow Li Diffusion in Spinel-Type Structured $Li_4Ti_5O_{12}$-A Comparison of Results from Solid State NMR and Impedance Spectroscopy. *Phys. Chem. Chem. Phys.* **2007**, *9*, 1239−1246.

(17) Xie, J.; Imanishi, N.; Matsumura, T.; Hirano, A.; Takeda, Y.; Yamamoto, O. Orientation Dependence of Li−Ion Diffusion Kinetics in $LiCoO_2$ Thin Films Prepared by RF Magnetron Sputtering. *Solid State Ionics* **2008**, *179*, 362−370.

(18) Shin, B. R.; Nam, Y. J.; Oh, D. Y.; Kim, D. H.; Kim, J. W.; Jung, Y. S. Comparative Study of TiS_2/Li-In All-Solid-State Lithium Batteries Using Glass-Ceramic Li_3PS_4 and $Li_{10}GeP_2S_{12}$ Solid Electrolytes. *Electrochim. Acta* **2014**, *146*, 395−402.

(19) Trevey, J. E.; Stoldt, C. R.; Lee, S. H. High Power Nanocomposite TiS_2 Cathodes for All-Solid-State Lithium Batteries. *J. Electrochem. Soc.* **2011**, *158*, 1282−1289.

(20) Whittingham, M. S. Electrical Energy Storage and Intercalation Chemistry. *Science* **1976**, *192*, 1126−1127.

(21) Long, P.; Xu, Q.; Peng, G.; Yao, X.; Xu, X. NiS Nanorods as Cathode Materials for All-Solid-State Lithium Batteries with Excellent Rate Capability and Cycling Stability. *ChemElectroChem* **2016**, *3*, 764−769.

(22) Cai, L.; Zhang, Q.; Mwizerwa, J. P.; Wan, H.; Yang, X.; Xu, X.; Yao, X. Highly Crystalline Layered VS_2 Nanosheets for All-Solid-State Lithium Batteries with Enhanced Electrochemical Performances. *ACS Appl. Mater. Interfaces* **2018**, *10*, 10053−10063.

(23) Shi, S.; Gao, J.; Liu, Y.; Zhao, Y.; Wu, Q.; Ju, W.; Ouyang, C.; Xiao, R. Multi-Scale Computation Methods: Their Applications in Lithium-Ion Battery Research and Development. *Chin. Phys. B* **2016**, *25*, 018212.

(24) Kang, J.; Han, B. First-Principles Characterization of the Unknown Crystal Structure and Ionic Conductivity of $Li_7P_2S_8I$ as a Solid Electrolyte for High-Voltage Li Ion Batteries. *J. Phys. Chem. Lett.* **2016**, *7*, 2671−2675.

(25) Kang, J.; Chung, H.; Doh, C.; Kang, B.; Han, B. Integrated Study of First Principles Calculations and Experimental Measurements for Li-Ionic Conductivity in Al-Doped Solid-State $LiGe_2(PO_4)_3$ Electrolyte. *J. Power Sources* **2015**, *293*, 11−16.

(26) Kohn, W.; Sham, L. J. Self-Consistent Equations Including Exchange and Correlation Effects. *Phys. Rev.* **1965**, *140*, 1133−1138.

DOI: 10.1021/acsami.8b12026
ACS Appl. Mater. Interfaces XXXX, XXX, XXX−XXX

(27) Dudarev, S. L.; Botton, G. A.; Savrasov, S. Y.; Humphreys, C. J.; Sutton, A. P. Electron-Energy-Loss Spectra and the Structural Stability of Nickel Oxide: An LSDA+U Study. *Phys. Rev. B: Condens. Matter Mater. Phys.* **1998**, *57*, 1505−1509.
(28) Heyd, J.; Scuseria, G. E.; Ernzerhof, M. Hybrid Functionals Based on a Screened Coulomb Potential. *J. Chem. Phys.* **2003**, *118*, 8207−8215.
(29) Monkhorst, H. J.; Pack, J. D. Special Points for Brillouin-zone Integrations. *Phys. Rev. B* **1976**, *13*, 5188−5192.
(30) Henkelman, G.; Uberuaga, B. P.; Jónsson, H. A Climbing Image Nudged Elastic Band Method for Finding Saddle Points and Minimum Energy Paths. *J. Chem. Phys.* **2000**, *113*, 9901.
(31) Baroni, S.; De Gironcoli, S.; Dal Corso, A.; Giannozzi, P. Phonons and Related Crystal Properties from Density-Functional Perturbation Theory. *Rev. Mod. Phys.* **2001**, *73*, 515−562.
(32) Togo, A.; Tanaka, I. First Principles Phonon Calculations in Materials Science. *Scr. Mater.* **2015**, *108*, 1−5.
(33) Wang, Y.; Richards, W. D.; Ong, S. P.; Miara, L. J.; Kim, J. C.; Mo, Y.; Ceder, G. Design Principles for Solid-State Lithium Superionic Conductors. *Nat. Mater.* **2015**, *14*, 1026.
(34) Mizuno, F.; Hayashi, A.; Tadanaga, K.; Tatsumisago, M. New, Highly Ion-Conductive Crystals Precipitated from Li_2S-P_2S_5 Glasses. *Adv. Mater.* **2005**, *17*, 918−921.
(35) Richards, W. D.; Wang, Y.; Miara, L. J.; Kim, J. C.; Ceder, G. Design of $Li_{1+2x}Zn_{1-x}PS_4$, A New Lithium Ion Conductor. *Energy Environ. Sci.* **2016**, *9*, 3272−3278.
(36) Liu, C. S.; Zhu, H. H.; Ye, X. J.; Yan, X. H. Prediction of A New BeC Monolayer with Perfectly Planar Tetracoordinate Carbons. *Nanoscale* **2017**, *9*, 5854−5858.
(37) Born, M.; Huang, K. *Dynamic Theory of Crystal Lattice*; Clarendon: Oxford, 1954; pp 120−154.
(38) Deng, Z.; Wang, Z.; Chu, I.-H.; Luo, J.; Ong, S. P. Elastic Properties of Alkali Superionic Conductor Electrolytes from First Principles Calculations. *J. Electrochem. Soc.* **2016**, *163*, 67−74.
(39) Makishima, A.; Mackenzie, J. D. Direct Calculation of Young's Moidulus of Glass. *J. Non-Cryst. Solids* **1973**, *12*, 35−45.
(40) Vitos, L.; Korzhavyi, P. A.; Johansson, B. Elastic Property Maps of Austenitic Stainless Steels. *Phys. Rev. Lett.* **2002**, *88*, 155501.
(41) Ong, S. P.; Wang, L.; Kang, B.; Ceder, G. Li−Fe−P−O_2 Phase Diagram from First Principles Calculations. *Chem. Mater.* **2008**, *20*, 1798−1807.
(42) Momma, K.; Izumi, F. VESTA 3 for Three-Dimensional Visualization of Crystal, Volumetric and Morphology Data. *J. Appl. Crystallogr.* **2011**, *44*, 1272−1276.
(43) Ning, F.; Li, S.; Xu, B.; Ouyang, C. Strain Tuned Li Diffusion in $LiCoO_2$ Material for Li Ion Batteries: A First Principles Study. *Solid State Ionics* **2014**, *263*, 46−48.
(44) Wei, Y.; Zheng, J.; Cui, S.; Song, X.; Su, Y.; Deng, W.; Wu, Z.; Wang, X.; Wang, W.; Rao, M.; Lin, Y.; Wang, C.; Amine, K.; Pan, F. Kinetics Tuning of Li-Ion Diffusion in Layered $Li(Ni_xMn_yCo_z)O_2$. *J. Am. Chem. Soc.* **2015**, *137*, 8364−8367.
(45) Ouyang, C.; Shi, S.; Wang, Z.; Huang, X.; Chen, L. First-Principles Study of Li Ion Diffusion in $LiFePO_4$. *Phys. Rev. B: Condens. Matter Mater. Phys.* **2004**, *69*, 104303.
(46) Winter, R.; Heitjans, P. Li^+ Diffusion and Its Structural Basis in the Nanocrystalline and Amorphous Forms of Two-Dimensionally Ion-Conducting Li_xTiS_2. *J. Phys. Chem. B* **2001**, *105*, 6108−6115.
(47) Van der Ven, A.; Thomas, J. C.; Xu, Q.; Swoboda, B.; Morgan, D. Nondilute Diffusion from First Principles: Li Diffusion in Li_xTiS_2. *Phys. Rev. B: Condens. Matter Mater. Phys.* **2008**, *78*, 104306.
(48) Hagenmuller, P.; Van. Gool, W. *Solid Electrolytes: General Principles, Characterization, Materials, Applications*, 1st ed.; Academic Press: New York, 1978; pp 217−233.
(49) Deng, Z.; Mo, Y.; Ong, S. P. Computational Studies of Solid-State Alkali Conduction in Rechargeable Alkali-Ion Batteries. *NPG Asia Mater.* **2016**, *8*, No. e254.
(50) Van der Ven, A.; Bhattacharya, J.; Belak, A. Understanding Li Diffusion in Li-Intercalation Compounds. *Acc. Chem. Res.* **2013**, *46*, 1216−1225.
(51) Mo, Y.; Ong, S. P.; Ceder, G. First Principles Study of the $Li_{10}GeP_2S_{12}$ Lithium Super Ionic Conductor Material. *Chem. Mater.* **2012**, *24*, 15−17.
(52) Ong, S. P.; Mo, Y.; Richards, W. D.; Miara, L.; Lee, H. S.; Ceder, G. Phase Stability, Electrochemical Stability and Ionic Conductivity of the $Li_{10\pm1}MP_2X_{12}$ (M= Ge, Si, Sn, Al or P, and X= O, S or Se) Family of Superionic Conductors. *Energy Environ. Sci.* **2013**, *6*, 148−156.
(53) Chevrier, V. L.; Ong, S. P.; Armiento, R.; Chan, M. K. Y.; Ceder, G. Hybrid Density Functional Calculations of Redox Potentials and Formation Energies of Transition Metal Compounds. *Phys. Rev. B: Condens. Matter Mater. Phys.* **2010**, *82*, No. 075122, DOI: 10.1103/PhysRevB.82.075122.
(54) Nakayama, M.; Yamada, S.; Jalem, R.; Kasuga, T. Density Functional Studies of Olivine-Type $LiFePO_4$ and $NaFePO_4$ as Positive Electrode Materials for Rechargeable Lithium and Sodium Ion Batteries. *Solid State Ionics* **2016**, *286*, 40−44.
(55) Yamada, A.; Koizumi, H.; Nishimura, S. I.; Sonoyama, N.; Kanno, R.; Yonemura, M.; Nakamura, T.; Kobayashi, Y. Room-Temperature Miscibility Gap in Li_xFePO_4. *Nat. Mater.* **2006**, *5*, 357.
(56) Luo, M.; Zhang, R.; Gong, Y.; Wang, M.; Chen, Y.; Chu, M.; Chen, L. Effects of Doping Al on the Structure and Electrochemical Performances of $Li[Li_{0.2}Mn_{0.54}Ni_{0.13}Co_{0.13}]O_2$ Cathode Materials. *Ionics* **2018**, *24*, 967−976.
(57) Suslov, E. A.; Bushkova, O. V.; Sherstobitova, E. A.; Reznitskikh, O. G.; Titov, A. N. Lithium Intercalation into TiS_2 Cathode Material: Phase Equilibria in a Li−TiS_2 System. *Ionics* **2016**, *22*, 503−514.
(58) Dahn, J. R.; Haering, R. R. Anomalous Bragg Peak Widths in Li_xTiS_2. *Solid State Commun.* **1981**, *40*, 245−248.
(59) Dathar, G. K. P.; Sheppard, D.; Stevenson, K. J.; Henkelman, G. Calculations of Li-Ion Diffusion in Olivine Phosphates. *Chem. Mater.* **2011**, *23*, 4032−4037.
(60) Li, W. J.; Hirayama, M.; Suzuki, K.; Kanno, R. Fabrication and Electrochemical Properties of a $LiCoO_2$ and $Li_{10}GeP_2S_{12}$ Composite Electrode for Use in All-Solid-State Batteries. *Solid State Ionics* **2016**, *285*, 136−142.
(61) Chen, C.; Guo, X. Space Charge Layer Effect in Solid State Ion Conductors and Lithium Batteries: Principle and Perspective. *Acta Chim. Slov.* **2016**, *63*, 489−495.
(62) Gao, J.; Zhao, Y.; Shi, S.; Li, H. Lithium-Ion Transport in Inorganic Solid State Electrolyte. *Chin. Phys. B* **2016**, *25*, 018211.
(63) Sakuda, A.; Hayashi, A.; Tatsumisago, M. Interfacial Observation between $LiCoO_2$ Electrode and Li_2S−P_2S_5 Solid Electrolytes of All-Solid-State Lithium Secondary Batteries Using Transmission Electron Microscopy. *Chem. Mater.* **2010**, *22*, 949−956.
(64) Zhang, Q.; Yao, X.; Mwizerwa, J. P.; Huang, N.; Wan, H.; Huang, Z.; Xu, X. FeS Nanosheets as Positive Electrodes for All-Solid-State Lithium Batteries. *Solid State Ionics* **2018**, *318*, 60−64.
(65) Xu, P.; Chen, S.; Huang, B.; Xiang, H. J.; Gong, X.-G.; Wei, S.-H. Stability and Electronic Structure of Cu_2ZnSnS_4 Surfaces: First-Principles Study. *Phys. Rev. B: Condens. Matter Mater. Phys.* **2013**, *88*, No. 045427, DOI: 10.1103/PhysRevB.88.045427.
(66) He, J.; Sun, L.; Zhang, K.; Wang, W.; Jiang, J.; Chen, Y.; Yang, P.; Chu, J. Effect of Post-Sulfurization on the Composition, Structure and Optical Properties of Cu_2ZnSnS_4 Thin Films Deposited by Sputtering from a Single Quaternary Target. *Appl. Surf. Sci.* **2013**, *264*, 133−138.
(67) Lepley, N. D.; Holzwarth, N. A. W.; Du, Y. A. Structures, Li^+ Mobilities, and Interfacial Properties of Solid Electrolytes Li_3PS_4 and Li_3PO_4 from First Principles. *Phys. Rev. B: Condens. Matter Mater. Phys.* **2013**, *88*, 104103.
(68) Chen, Y.; Cai, L.; Liu, Z.; Dela Cruz, C. R.; Liang, C.; An, K. Correlation of Anisotropy and Directional Conduction in β-Li_3PS_4 Fast Li^+ Conductor. *Appl. Phys. Lett.* **2015**, *107*, 013904.
(69) Kahn, A. Fermi level, Work Function and Vacuum Level. *Mater. Horiz.* **2016**, *3*, 7−10.
(70) Aras, M.; Kılıç, Ç.; Ciraci, S. Planar Heterostructures of Single-Layer Transition Metal Dichalcogenides: Composite Structures,

DOI: 10.1021/acsami.8b12026
ACS Appl. Mater. Interfaces XXXX, XXX, XXX−XXX

Schottky Junctions, Tunneling Barriers, and Half Metals. *Phys. Rev. B: Condens. Matter Mater. Phys.* **2017**, *95*, No. 075434, DOI: 10.1103/PhysRevB.95.075434.

DOI: 10.1021/acsami.8b12026
ACS Appl. Mater. Interfaces XXXX, XXX, XXX−XXX